Numerical modeling of Surface-Scan MRI experiments for improved diagnostics of commercial battery cells

Konstantin Romanenko, Alexej Jerschow

▶ **To cite this version:**

Konstantin Romanenko, Alexej Jerschow. Numerical modeling of Surface-Scan MRI experiments for improved diagnostics of commercial battery cells. Journal of Magnetic Resonance Open, 2022, 10-11, pp.100061. 10.1016/j.jmro.2022.100061 . cea-03654405

HAL Id: cea-03654405

https://cea.hal.science/cea-03654405

Submitted on 28 Apr 2022

HAL is a multi-disciplinary open access archive for the deposit and dissemination of scientific research documents, whether they are published or not. The documents may come from teaching and research institutions in France or abroad, or from public or private research centers.

L'archive ouverte pluridisciplinaire **HAL**, est destinée au dépôt et à la diffusion de documents scientifiques de niveau recherche, publiés ou non, émanant des établissements d'enseignement et de recherche français ou étrangers, des laboratoires publics ou privés.

Distributed under a Creative Commons Attribution - NoDerivatives 4.0 International License

Journal of Magnetic Resonance Open 10–11 (2022) 100061

Contents lists available at ScienceDirect

Journal of Magnetic Resonance Open

journal homepage: www.sciencedirect.com/journal/journal-of-magnetic-resonance-open

Numerical modeling of Surface-Scan MRI experiments for improved diagnostics of commercial battery cells

Konstantin Romanenko [a,*], Alexej Jerschow [b]

[a] CEA Saclay, Laboratoire Structure et Dynamique par Résonance Magnétique, 91191, Gif-sur-Yvette, France
[b] Department of Chemistry, New York University, 100 Washington Square East, 10003, New York, NY, USA

ARTICLE INFO

Keywords:
SPRITE
COMSOL
Numerical modeling
Io-MRI
Jelly-roll cells
Battery diagnostics

ABSTRACT

Recent progress in MRI methods development led to a novel concept for operando screening of commercial battery cells. Sensing electrochemical processes inside an operating cell can be done via the detection of associated magnetic fields. This concept is based on the classic phenomenon described by Ampère's circuital and Biot–Savart laws. A new method referred to as Surface-Scan MRI employs ultra-fast quantitative mapping of the magnetic field in a thin layer of polymer placed in direct contact with the cell. Preliminary experimental work demonstrated the ability of Surface-Scan MRI to detect cells that undergone overcharging, a hazardous event that can degrade cells' components and ultimately creates a risk of fire. In the future, the analysis of Surface-Scan MRI data can rely largely on numerical simulations of electromagnetic phenomena based on accurate models of real cells. A series of numerical tests performed in this work confirms the capacity of Surface-Scan MRI to detect a variety of defects associated with electrochemical degradation of cathode, anode and electrolyte materials. Effects of morphology, location and conductivity of the defects on magnetic field distributions were examined for realistic cell models including flat jelly roll configurations. MRI resolution limits associated with the defect domain size and with the distance between the defect and the detection medium were estimated. Location and morphology of highly conductive defects ($\sigma > 10^5$ S m^{-1}), *e.g.* regions rich in quasi-metallic dendrites, can be directly identified from Surface-Scan MRI images. Low conductivity defects , *e.g.* degraded electrolyte or cathode and anode coatings, manifest via patterns much larger than the defects.

1. Introduction

Lithium-ion technology remains the most efficient approach for electrochemical energy storage for the foreseeable future, and will most likely play a dominant role in the rapidly growing electric vehicle (EV) market. However, the EV and Li-ion industries have to accommodate safety concerns associated with high energy density and flammability of lithium-ion batteries. Knowledge of potential failures in commercial electrochemical cells and understanding of the underlying mechanisms of these events [1–12] can enable improved battery designs and safety. Various high risk scenarios can occur over a cell's life cycle and lead to hazardous events like fires [13]. Specifically, violation of manufacturing protocols and random errors can occur during high throughput processes. As a result, numerous defective cells can be released to the market. Deployment of reliable and time-efficient battery screening technologies is expected to significantly reduce risks posed by such cells.

Nuclear magnetic resonance spectroscopy (NMR) and magnetic resonance imaging (MRI) methods enabled nondestructive *in situ* and *operando* studies of fundamental electrochemical processes [14]. In addition to NMR spectroscopy of NMR - compatible cell prototypes, a few MRI - based strategies have been proposed for visualization of electrochemical phenomena in commercial battery cells [15–18]. A concept of inside-out (io) MRI was introduced to address concerns associated with safety of Li-ion cells [15,16]. A cell placed in a uniform magnetic field (MF) would produce a MF perturbation associated with the distribution of magnetic susceptibility inside the cell.

Later, io-MRI was adapted for characterization of direct currents (DC) circulating inside operating Li-ion cells [17,18]. Surface-Scan MRI [18], a recent advance in io-MRI methodology, demonstrated high sensitivity to potentially hazardous cell states resulting from violation of operating specifications. MF of an operating cell is measured using a 2-dimensional (2D) Single Point Ramped Imaging with T_1 enhancement

Abbreviations: SPRITE, Single Point Ramped Imaging with T_1 enhancement; io-MRI, Inside-Out MRI.

* Corresponding author.
E-mail address: konstantin.romanenko@cea.fr (K. Romanenko).

https://doi.org/10.1016/j.jmro.2022.100061
Received 26 February 2022; Received in revised form 5 April 2022; Accepted 22 April 2022
Available online 23 April 2022
2666-4410/© 2022 The Author(s). Published by Elsevier Inc. This is an open access article under the CC BY-NC-ND license (http://creativecommons.org/licenses/by-nc-nd/4.0/).

(SPRITE) [19]. This method doesn't suffer from misregistration ('susceptibility') artifacts that are common for MRI techniques based on frequency encoding [20–22]. The proton signal is provided by a thin layer of Plastisol (PVC - based polymer), a safe, flexible and commercially viable solid-state detection medium device. By placing it in direct contact with the cell, the most intense MF perturbations can be detected, thus ensuring a maximum sensitivity for a given current. A rapid 2D acquisition (< 4 s) ensured negligible variations in the state of charge (SoC) during the signal acquisition. This approach in turn allowed much higher operational currents and, as a result, a higher sensitivity [18] as compared to 3D io-MRI [16, 17].

Surface-Scan MRI can be one of the most promising battery diagnostic methods to date. Its wide-scale implementation would benefit from an experimental database serving as a "biometric archive" for batteries. Although such a database can be acquired within realistic time frames, establishing MF patterns theoretically based on known cell designs and common failure modes should be considered. In this preliminary study, we attempt to validate the Surface-Scan MRI concepts by modeling electromagnetic fields of operating cells (e.g. flat jelly roll and prismatic designs) using COMSOL Multi-physics. Malfunctioning cells were modeled by introducing defect domains varying in size, spatial pattern, and conductivity.

2. Methods

2.1. Surface-Scan MRI concept

A magnetic field perturbation, ΔB, created by a battery cell can be described as a superposition of several independent terms:

$$\Delta B = B_{ST} + B_{SoC} + B_{DC} \quad (1)$$

where B_{ST} is a static field perturbation associated with geometrical configurations of the magnetic cell components, *e.g.* magnetic tabs, terminals and electrodes; B_{SoC} is a component associated with SoC or oxidation state - dependent magnetic susceptibilities of active cathode and anode materials; and B_{DC} is the DC-induced MF component, a function of the current density distribution. Note, B_{DC} also depends on SoC [17, 18].

All terms in Equation1 can be sensitive to mechanical, corrosive and electrochemical degradation of a cell. Certain hazardous battery cell lifecycle events (*e.g.* local electrolyte decomposition or copper migration) are not expected to alter B_{ST} and B_{SoC} maps noticeably. Such cells examined in a resting state could, therefore, pass an io-MRI screening. The B_{DC} term is a unique io-MRI metric associated with electrochemical processes in an operating cell. Specifically, B_{DC} is sensitive to current density variations resulting from degradation of electrode materials on a microscopic level, *e.g.* growth of dendrites, copper migration and electrolyte decomposition. Some of these processes are known to result in internal shorts and thermal runaway.

A net B_{DC} effect produced by a cell operating at a current I for a given SoC can be obtained as:

$$B_{DC}(SoC, I) = \Delta B(SoC, I) - \Delta B(SoC, 0), \quad (2)$$

where $\Delta B(SoC, I)$ is MF perturbation produced by the operating cell, and $\Delta B(SoC, 0)$ is a "reference" image, i.e. a MF perturbation produced by the cell in the rest state.

A new quantitative indicator of cell degradation was introduced in Ref.18:

$$\Delta B_{DC} = B_{DC} - B_{DC}{}^{S}, \quad (3)$$

ΔB_{DC} is a map of B_{DC} field deviation from a standard pattern B_{DC}^{S} established for a "healthy" fully charged cell (SoC = 100%). The B_{DC} term was shown to vary minimally within a safe range of SoCs from ~ 20 to ~ 100%. Thus, ΔB_{DC} of a healthy cell is largely a featureless "noisy" image. Overcharging of cells led to the formation of ΔB_{DC} patterns varying in size from mm's to cm's. These spatially sporadic ΔB_{DC} features were referred to as "memory effects" since they had not vanished after the cells were discharged to within the safe SoC range [18]. Note, since ΔB_{DC} scales linearly with the current, ΔB_{DC} maps could be normalized by the current magnitude. The normalization would provide a current-independent metric describing the defect domain.

The experimental surface-scan MRI approach is based on the Centric-Scan SPRITE technique described in the previously published articles [16–18]. Sampling several consecutive complex data points per gradient step in a single SPRITE acquisition allows one to reconstruct several purely phase-encoded images, and scale their fields-of-views (FOV) using a chirp-z transform algorithm [19]. These data represent a temporal evolution of spatially resolved MR phase, $\varphi(\boldsymbol{r}, T_P)$. The phase encoding time, T_P^k, of the k^{th} complex data point is determined as $T_P^k = T_P^{min} + (k\text{-}1)\ SW^{-1}$, where T_P^{min} and SW are a minimum phase encoding time and the sampling bandwidth, respectively. The range of T_P's achieved in the experimental work was from 114 to 170 μs [18] which enabled detection of strongly attenuated ^{1}H MRI signals.

Temporal phase evolution is driven by local Larmor frequency offsets $\gamma\Delta B_0(\boldsymbol{r})$. Experimental MF maps are reconstructed by pixel-by-pixel linear regression of the temporal phase evolution $\varphi(T_P)$:

$$\Delta B_0(r) = \gamma^{-1}\Delta\phi(\boldsymbol{r}, T_P)/\Delta T_P, \quad (4)$$

2.2. Cell modeling

In the most simple case, a cell is modeled as a stack of rectangular 50 μm thick sheets made of aluminum, cathode coating, electrolyte, anode coating and copper. The dimensions of the cell are: length $D_Z = 3.5$ cm, width $D_X = 2.0$ cm, and thickness $D_Y = 0.25$ mm. This design is further referred to as a "single-layer" cell. The Z-axis is aligned with the measurable component of the magnetic field (B_Z), which represents the direction of the external magnetic field (B_0) in experimental Surface-Scan MRI settings. In addition to the single-layer cell, flat jelly roll models containing 3, 5 and 7 layers are examined. The dimensions of these cells are $D_Z = 3.5$ cm, $D_X = 2.0$ cm, and D_Y varies between 0.85 and 2.05 mm. The jelly roll configurations are common in commercial "pouch" and "prismatic" cells. A cell comprising an odd number of layers allows placing the positive and negative tabs further apart. Such an arrangement of the tabs results in a reduced risk of short-circuit while engaging the maximum area of the electrodes.

Fig. 1a–c show *X-Z, Y-Z*, and *X-Y* views of the 5-layer (2.5 turns) cell. Curved regions of the layers are approximated with semicircular fragments 'extruded' along *Z*, Fig. 1d). Cell terminals (tabs) are designed as extensions of the corresponding current collectors (Al and Cu) and approximated by rectangular plates 3 mm (X) × 1 mm (Z) × 50 μm (Y). The tabs, Fig. 1a), are placed at the bottom of the cell and separated by 1.4 cm along the X dimension. The 3- and 7-layer cells are constructed in a similar manner. These are realistic models of commercial cells used in portable electronics, and they can be easily up-scaled in order to approximate EV cells.

Conductivities (σ) of aluminum and copper current collectors are assigned 3.5×10^7 and 6×10^7 S m^{-1}, respectively (COMSOL materials library). Across a broad range of electrochemically active materials, conductivities of cell components vary by several orders of magnitude from 10^{-9} to 10^3 S m^{-1} in cathode materials, and from 10^4 to 10^6 S m^{-1} in anodes based on graphitized carbon. Ionic conductivities of electrolytes rarely exceed 10 S m^{-1} [23]. To approximate a graphite - based anode, electrical conductivity and relative permittivity are assigned the values of 10^5 S m^{-1} and 10, respectively [24,25]. Cathodes of Li-ion cells are usually composed of an electrochemically active material (multi--metal oxides), a binder (*e.g.* Polyvinylidene Fluoride - PVDF), and a conductive additive (a porous material based on Carbon Black or carbon nanotubes). The additive provides a transport network for rapid electron transfer between the active material and the current collector. An

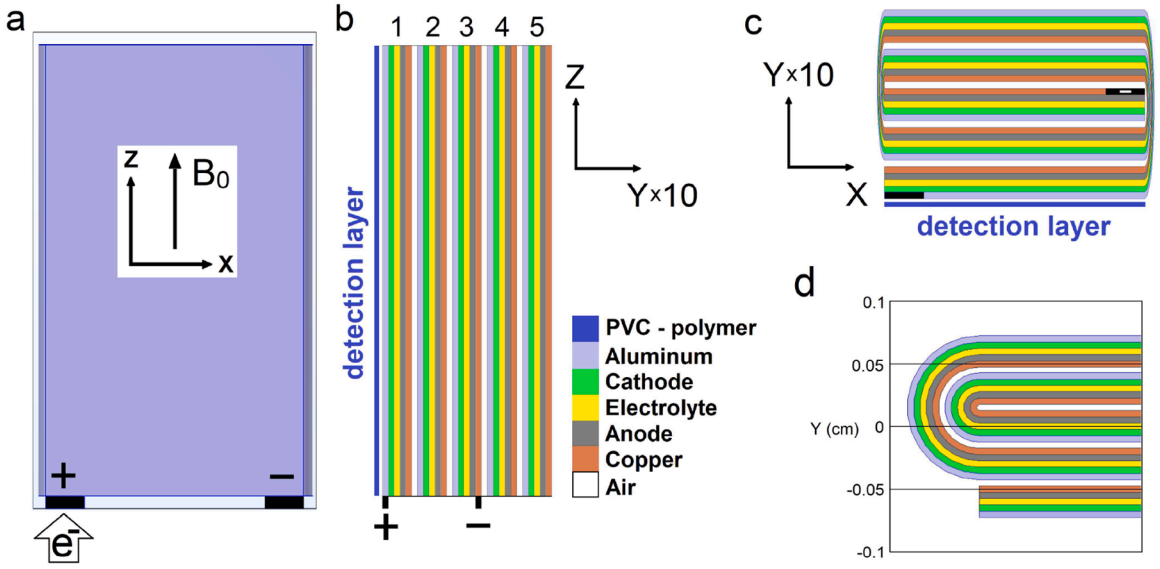

Fig. 1. A design of a 5-layer (2.5 turns) jelly-roll cell developed in COMSOL for simulations of magnetic field and current density distributions: (a) X-Z, (b) Y-Z and (c) X-Y views. The Y dimension is shown at × 10 the real scale. Insets indicate conventions related to spatial directions (X, Y, Z). Cell layer numbering convention and materials of the cell components are provided in (b). The location of the detection medium layer is indicated in (b) and (c). The detailed geometry of the cell layer folding is shown in (d).

overall current density in the composite cathode coating is limited by slow solid-state ion transport, interfacial ion transport, and by relatively low electronic conductivity of the active material. In this study, the conductivity and the relative permittivity of the composite cathode coating is assigned a value of 1 S m^{-1} and 1, respectively. Electrolyte's conductivity (ionic) and relative permittivity are assigned values of 1 S m^{-1} and 10, respectively. Conductivity and permittivity values of the COMSOL cell models are within ranges encountered in common electrochemical materials [23, 26–30].

Defective cells are modeled by adding various defect domains into standard cell configurations described above. A defect domain is defined in this study as parts of the cell where conductivities deviate from the standard values. In general, a defect domain can be characterized by a spatial distribution of conductivity. For simplicity in this study, the conductivity of the defect domain is constant over the domain.

2.3. Simulations

COMSOL (v.5.6) simulations were performed using *AC/DC* module (*Electromagnetic Fields* > *Vector Formulations* > *Magnetic and Electric Fields*). In the stationary case, current density and associated magnetic field distributions are described with the following Eqs. (5–9):

$$\nabla \times H = J, \tag{5}$$

$$B = \nabla \times A, \tag{6}$$

$$J = \sigma E, \tag{7}$$

$$\nabla \cdot J = 0, \tag{8}$$

$$E = -\nabla V, \tag{9}$$

Here H - magnetic field intensity, J - current density, E - electric field intensity, B - magnetic flux density, A - magnetic vector potential, V - electric scalar potential. The COMSOL algorithm solves Ampère's law (Eq. (4)) for the magnetic vector potential (A) together with a current conservation equation (Eq. (7)) for the electric potential (V).

The computation time varied between 15 min and 160 h depending on the number of layers in a cell model. Simulations of Surface-Scan MRI data for larger multi-turn cells (number of layers > 7) require significant computational resources.

3. Results and discussion

3.1. Reference maps

By design, a Surface-Scan MRI measurement provides a 2D map of the Z - component of magnetic field (B_Z) in the plane (X-Z) adjacent to the cell. In practice, the solid-state detection medium has a finite width ~ 1 mm (controlled by MRI sensitivity), and a local $B_Z(x, z)$ value is a result of averaging along the Y dimension. B_{DC} field distributions were simulated within a volume 2.2 (X) × 2 (Y) × 3.7 (Z) cm^3. The observation slice 2 (X) × 3.5 (Z) is selected at a 1 μm distance from the aluminum current collector, Fig. 1b and c.

In the original Surface-Scan MRI experiments [18], a 4 A DC pulse switched on for ~ 3.5 s provided excellent sensitivity. Cells were examined in the discharge mode which allowed the total voltage values to be within an operational range of the potentiostat (5 V). Thus, in all MF simulations presented below, a 4 A discharge current is implemented. Here, we use the convention of a 'positive' current I driven in the direction opposite to the movement of electrons. During discharging, electrons enter the tab of the cathode (+), Fig. 1a.

2D maps of B_{DC} field generated by 1-, 3-, 5- and 7-layer cells are shown in Figs. 2a-d, respectively. Histograms of these MF distributions are provided in Fig. 3a–d. The mean B_{DC} value, $\langle B_{DC} \rangle$, varies from 52 to 241 μT. The strongest field is generated near cell terminals and varies from 1.3 mT in the 1-layer cell to 1.8 mT in the 7-layer cell. Full 3D simulations of the B_{DC} field provide an estimation of magnetic field averaging that would occur over a finite width of the detection medium. This information would improve the interpretation of experimental Surface-Scan MRI data. B_{DC} distributions in the central Y-Z slice have a quasi-antisymmetric pattern Fig. 4. The symmetry of a B_{DC} pattern is partly controlled by an average direction of the current, i.e. along the line connecting the terminals. The line, in fact, is not parallel to the X direction, Fig. 1c. As the number of turns increases, Y-Z patterns become more asymmetric, Fig. 1S (Supporting Information - SI).

3.2. ΔB_{DC} metrics

In the following subsections, ΔB_{DC} distributions (Equation3) are

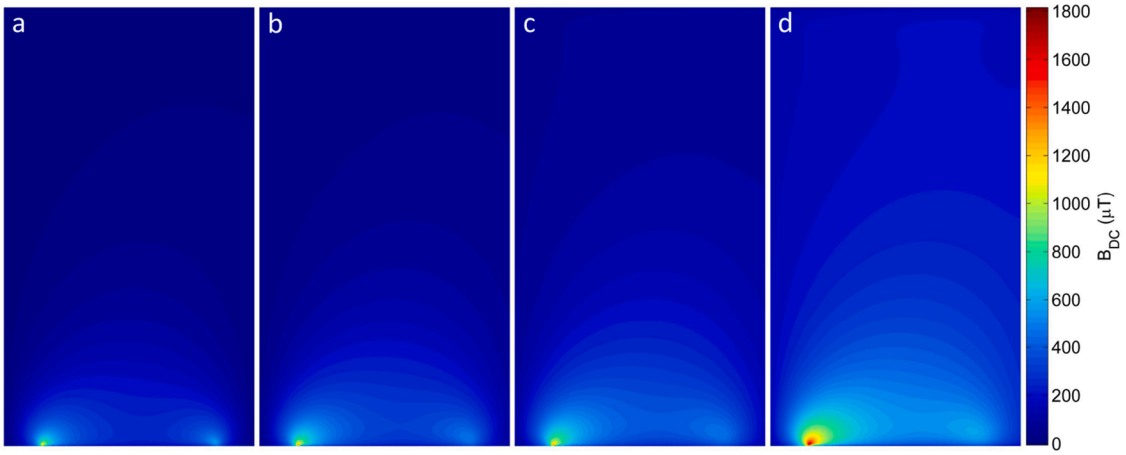

Fig. 2. 2D maps (X-Z) of B_{DC} - field simulated for 1- (a), 3- (b), 5- (c) and 7-layer (d) cells. The plane of the image is located at a distance of 1 μm from the cathode's current collector. The image FOV is 2 cm (X) × 3.5 cm (Z).

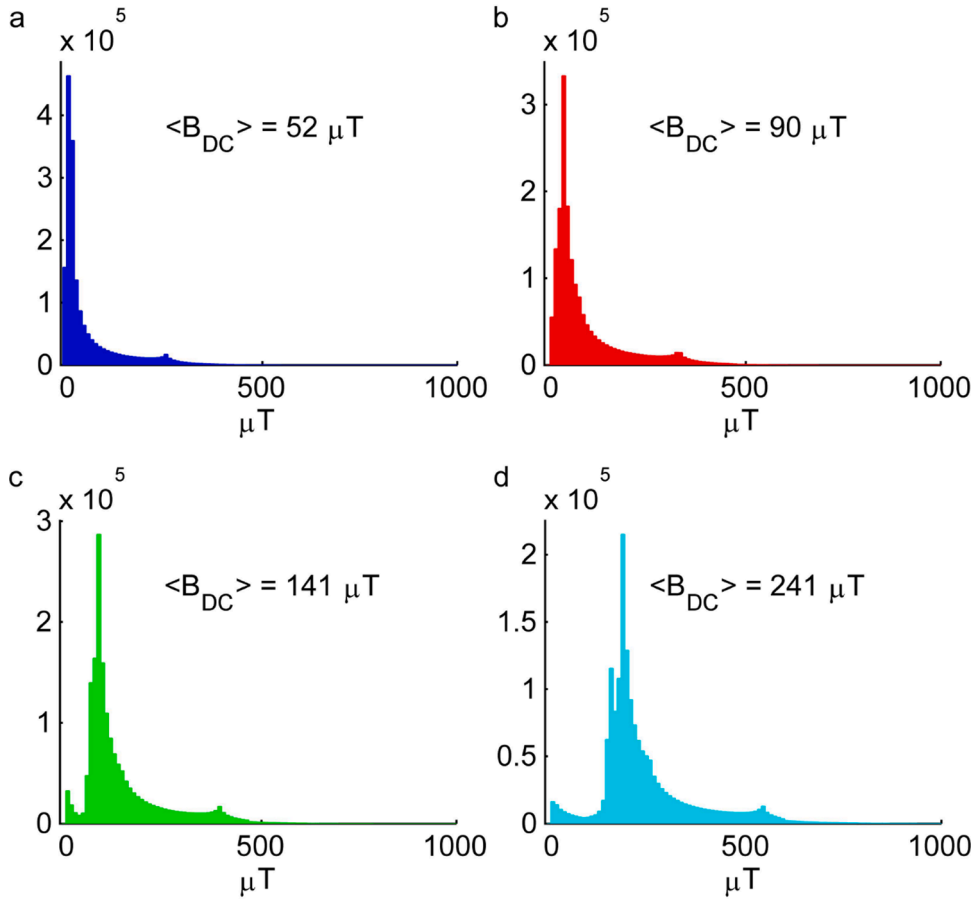

Fig. 3. Histograms of B_{DC} - field distributions simulated for 1- (a), 3- (b), 5- (c) and 7-layer (d) cells. Corresponding mean B_{DC} values are 52, 90, 141 and 241 μT, respectively.

examined with respect to such attributes of the defect domain as morphology, dimensions, location, and conductivity. B_{DC} maps of "defect-free" cells (Fig. 2) are used as reference images (B^{S}_{DC}) in Equation3.

3.2.1. *Defect morphology*

Fig. 5 shows ΔB_{DC} maps resulting from several geometries of the defect domain: disk (a), right triangular prism (b) and square prism (c). In each case, a given prismatic geometry is confined within the cathode and electrolyte layers and its base is parallel to the X-Z plane, Fig. 5d. The diameter of the disk, and the side lengths of the triangle and the square are 4 mm. The conductivity in these domains is assigned a value $\sigma = 10^7$ S m^{-1} significantly higher than the nominal values in the rest of the cathode and electrolyte. These defects approximate macroscopic domains containing highly conductive impurities, *e.g.* Li metal dendrites.

ΔB_{DC} patterns resulting from an array of 9 square prisms ($\sigma = 10^7$ S m^{-1}) distributed on a uniform grid are shown in Fig. 6a–d. ΔB_{DC} maps

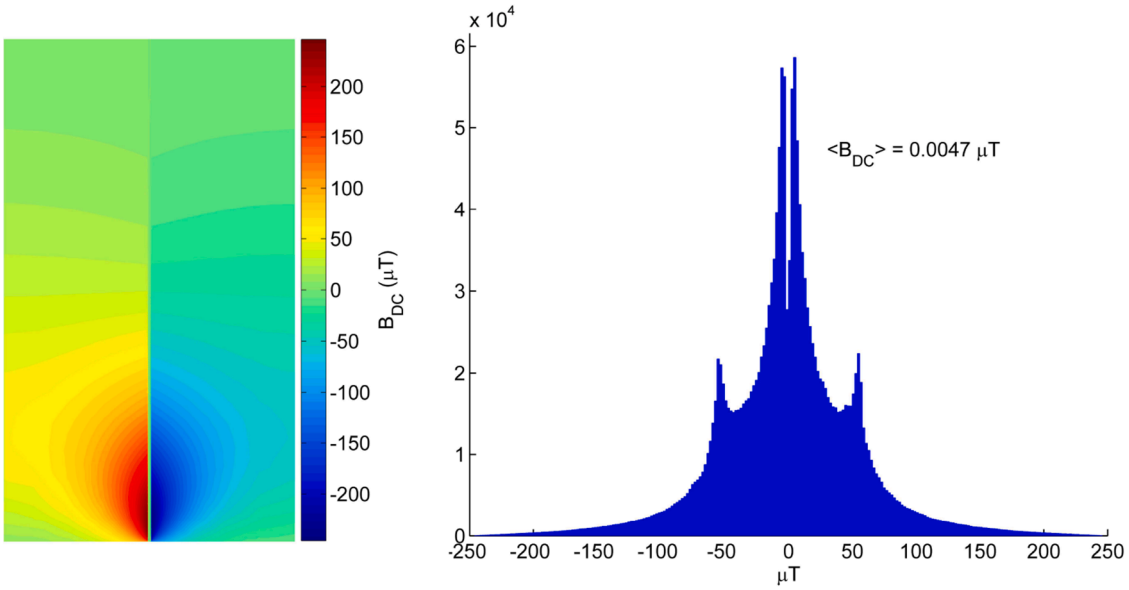

Fig. 4. A map of B_{DC} - field distribution in the central Y-Z plane (left) simulated for an operating 1-layer cell. FOV is 2 cm (Y) × 3.5 cm (Z). A histogram of the B_{DC} distribution is shown on the right.

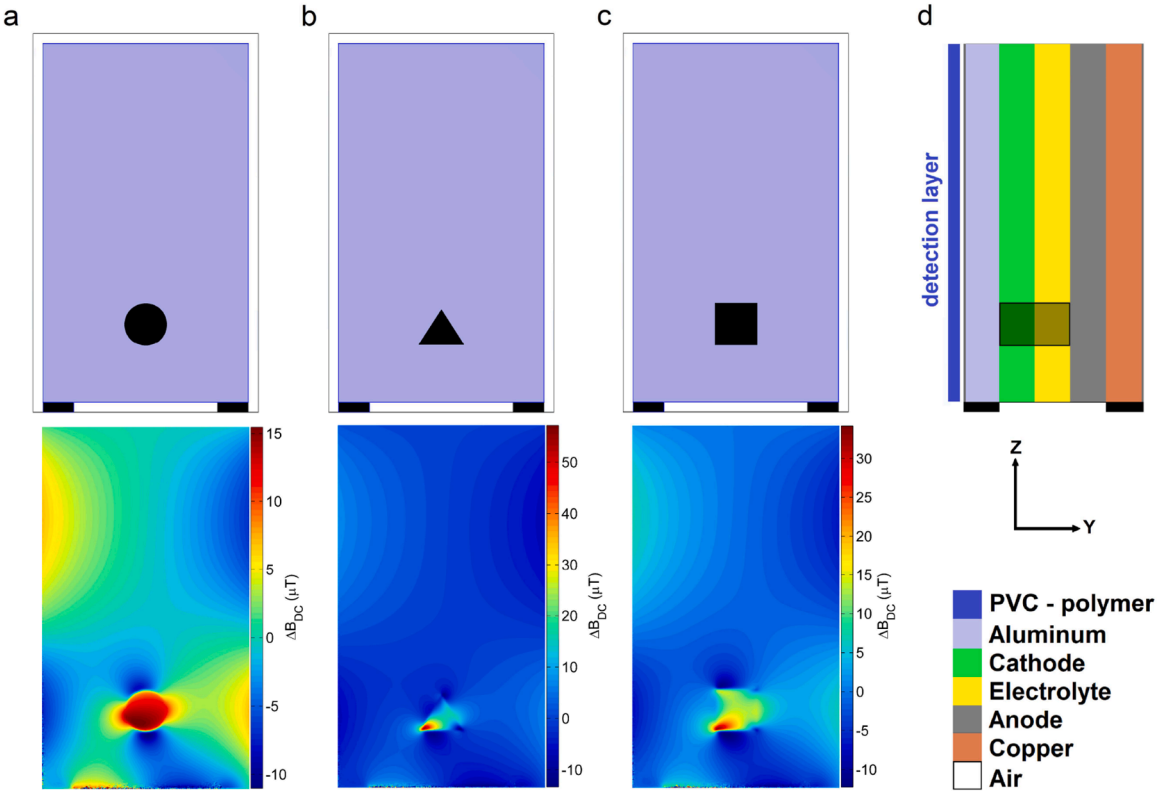

Fig. 5. ΔB_{DC} patterns resulting from defect domains in a form of disk (a), right triangular prism (b) and square prism (c). In each case, a given prismatic geometry is confined within the cathode and electrolyte layers and its base is parallel to the X-Z plane (d). The diameter of the disk, and the side lengths of the triangle and the square are 4 mm.

were simulated for defect sizes (d_x-d_z) of 0.2, 0.5, 1 and 2 mm. Coordinates of the defect centers with respect to the center of the X-Z pane are: Z(−1, 0, +1 cm) and X(−0.5, 0, 0.5 cm). The ΔB_{DC} magnitude drops off rapidly with the distance from a defect to the positive tab and with the size of the defect. Since a practical SPRITE resolution is close to 1 mm, identification and analysis of defect domains much smaller than 1 mm would be difficult. Specifically, ΔB_{DC} features resulting from microscopic defect domains would be misrepresented and blurred due to partial volume effects. Fig. 6e–h demonstrate how partial volume effects would affect the ΔB_{DC} data shown in Fig. 6a-d if MRI resolution was 1 mm. Fig. 6 illustrates the ability of Surface-Scan MRI to resolve defect domains with high (10^7 S m^{-1}) conductivity. Based on initial experimental work [18], it is apparent that domains smaller than 0.2 mm would be hard to detect due to low signal-to-noise ratio. Note, although

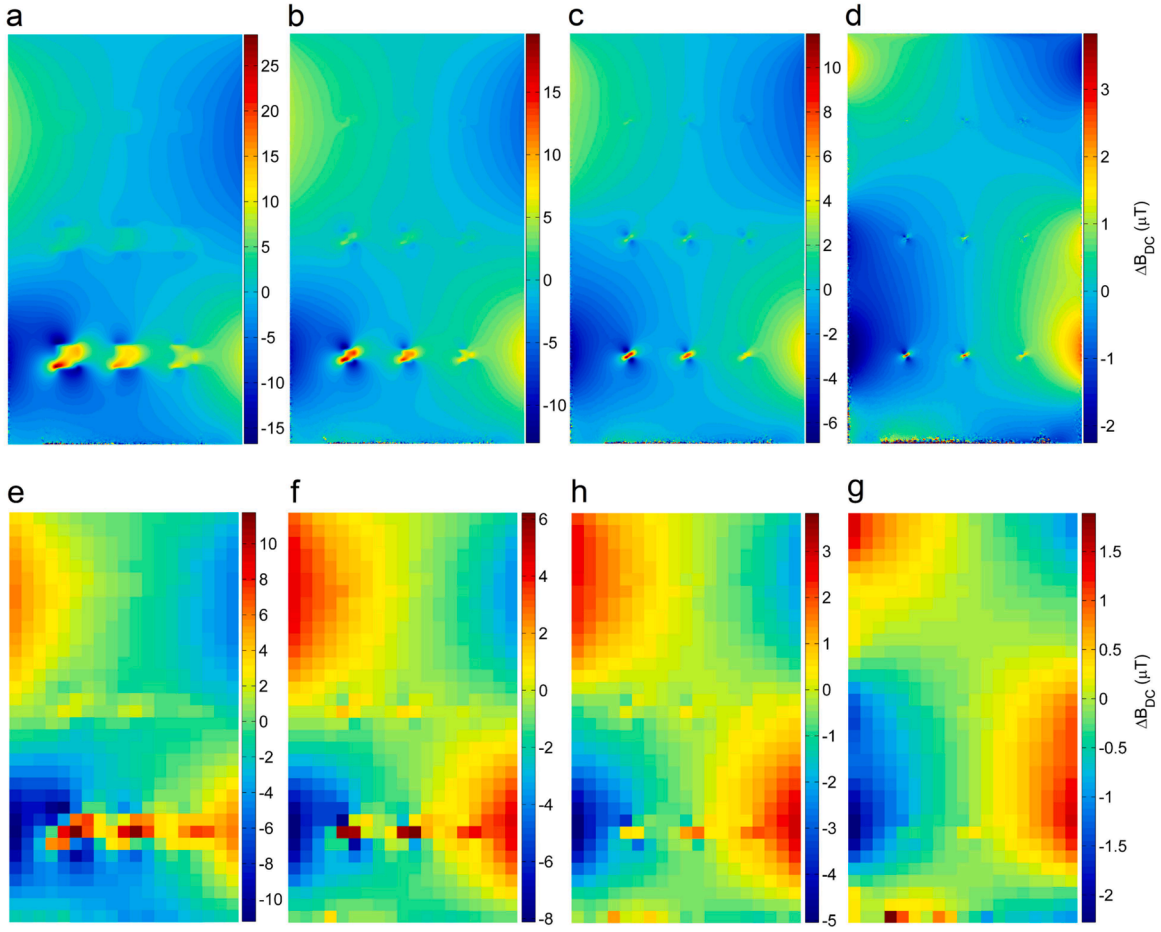

Fig. 6. ΔB_{DC} patterns (a-d) resulting from defect domains designed as arrays of 9 square prisms ($\sigma = 10^7$ S m^{-1}). Domain elements are distributed on a uniform grid within the electrolyte and cathode coating. X-Z coordinates of the domain elements with respect to the center of the cell are: Z(−1, 0, +1 cm) and X(−0.5, 0, 0.5 cm). Dimensions d_x, d_z (mm) of the domain elements: (a) 2, (b) 1, (c) 0.5 and (d) 0.2. (e–g) ΔB_{DC} maps resulting from partial volume effects (1 mm spatial resolution) applied to images (a-d).

the fine defects cannot be resolved, *e.g.* Fig. 6g, they still manifest as ~ 1–2 cm half-ovals near the periphery of the image.

3.2.2. *Location of the observation slice*

The ability to identify the morphology of a defect domain based on its ΔB_{DC} pattern depends on the distance (D_0) between the cell surface and the observation plane. Image blurring effects resulting from a series of D_0's are demonstrated for the disk shaped defect domain, Fig. 7. The ΔB_{DC} maps are shown in a region-of-interest (ROI) of 15 × 15 mm. Increasing the distance between the measurement plane and the cell's surface from 1 μm to 1 mm results in $a \approx 2.5$ fold reduction in ΔB_{DC} peak values. Although such blurring is inevitable, the resolution enhancement can be achieved with a thinner (< 0.5 mm) detection layer. An associated loss in sensitivity can be partially obviated by means of high proton density materials. A fluorine containing detection medium in combination with ^{19}F MRI resonators can also be employed.

3.2.3. *Defects inside a jelly roll cell*

A convention for cell layer numbering used below implies that the layer's number increases with the distance from the observation plane, Fig. 1b. Effects of the defect position in a 5-layer jelly roll cell are shown in Fig. 8. A high conductivity 4 mm diameter disk placed in the cathode and the electrolyte, Fig. 8a and b of layers #1 – #5 results in ΔB_{DC} patterns displayed in Fig. 8c–g, respectively. The X-Z coordinates of the

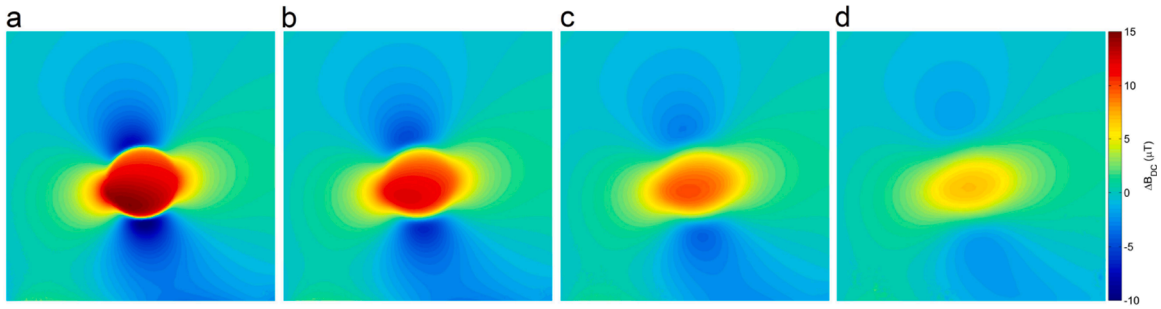

Fig. 7. ΔB_{DC} maps of the disk shaped defect domain within the electrolyte and cathode coating at D_0's of (a) 1um, (b) 0.2 mm, (c) 0.5 mm and (d) 1 mm. The displayed region-of-interest (ROI) is 15 × 15 mm.

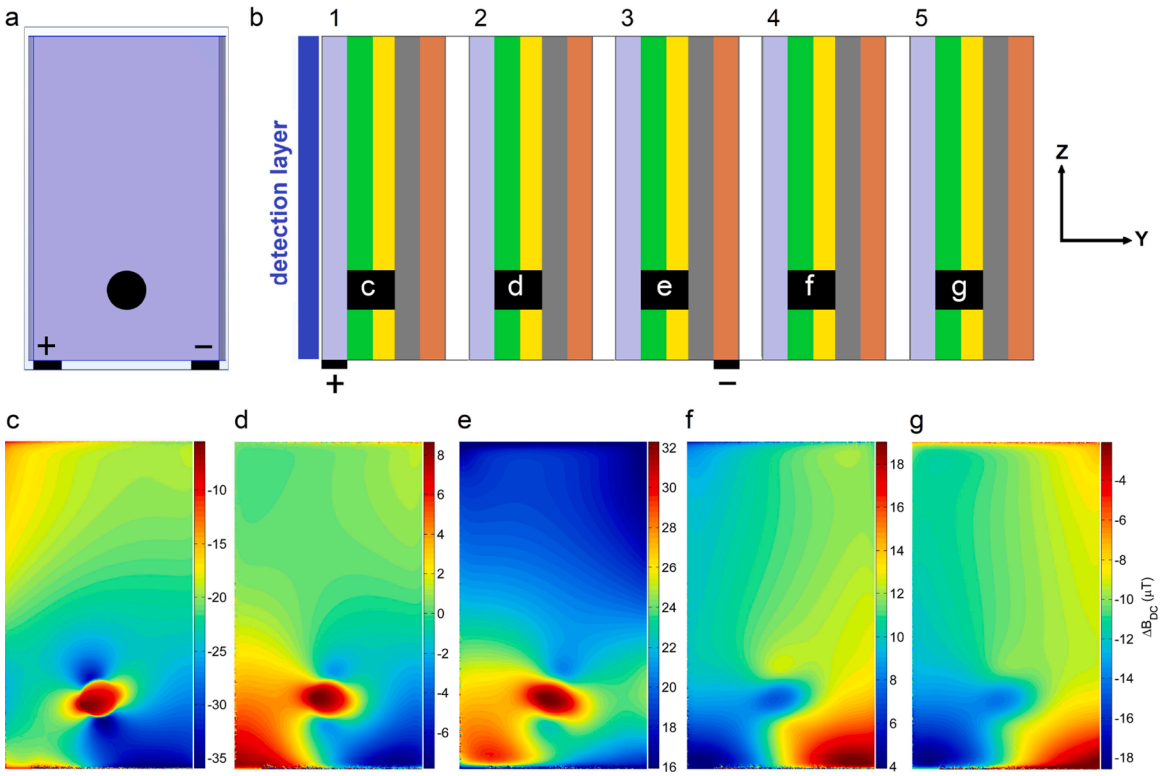

Fig. 8. (a, b) A schematic of the 5-layer jelly-roll cell; X-Z (a) and Y-Z (b) views. Dimensions of the cell: $D_X = 2.0$ cm, $D_Z = 3.5$ cm and $D_Y = 1.45$ mm. Defect domain is a 4 mm diameter disk ($\sigma = 10^7$ S m^{-1}) located in cathode and electrolyte regions. In the X-Z plane, the center of the circle is located 1 cm below the center of the cell. (c–g) ΔB_{DC} distributions corresponding to defect locations indicated in (b).

defect domains are the same as in Fig. 5a.

Defect domains located in different layers of the jelly roll cell manifest in a manner similar to the single layer cell. It is apparent that for the defect in the first layer, Fig. 8c an overall ΔB_{DC} variation (*i.e.* method's sensitivity) is the largest, and the shape of the defect is reproduced by magnetic field most accurately. The ΔB_{DC} representation of the 'circle', however, degrades as the defect is placed farther away from the detection medium, Fig. 8d–g. Apparently, Surface-Scan MRI provides the highest sensitivity to defects located in the outer cell layers. If implemented in a high-throughput process, scanning both sides of a flat cell

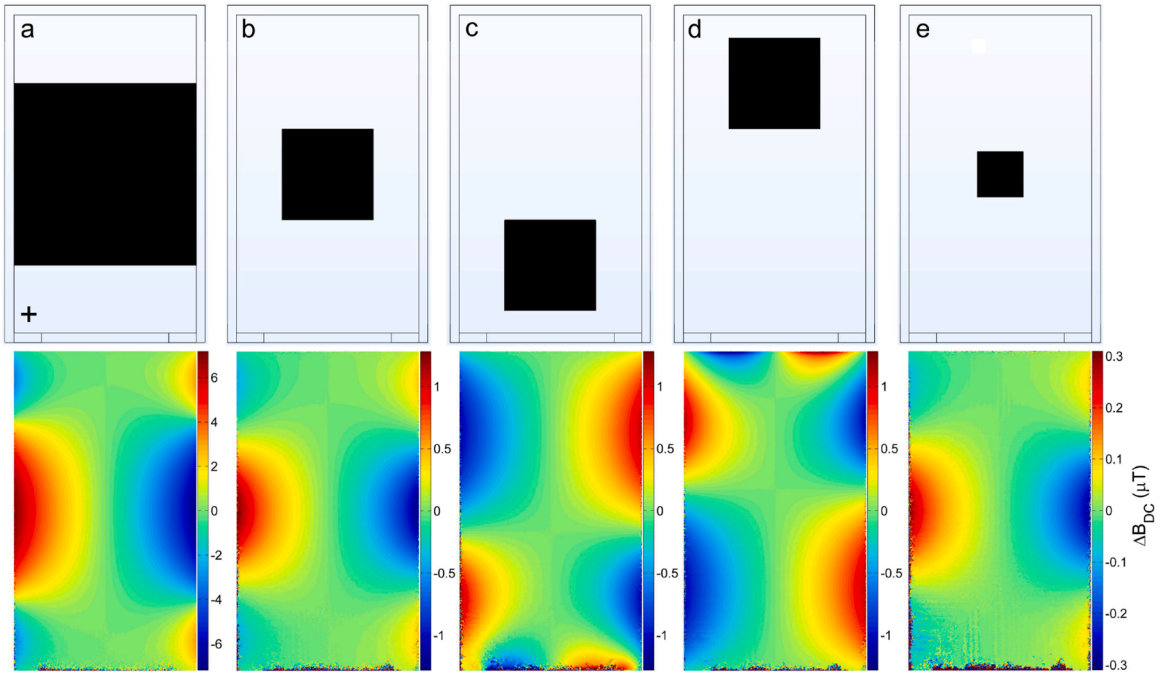

Fig. 9. Models of 1-layer cells (X-Z views) including domains of defective cathode coating (square prisms, $\sigma = 10^{-2}$ S m^{-1}) with reduced conductivity (top row), and corresponding ΔB_{DC} distributions (bottom row). Dimensions of square regions (cm) are (a) 2, (b–d) 1, and (e) 0.5.

would significantly improve the diagnostic accuracy of Surface-Scan MRI.

3.2.4. Defects of cathode coating

A 'failed' coating process could result in low conductivity regions in the cathode coating. Fig. 9 demonstrates magnetic field effects induced by such defects in the single layer cell. Conductivity in these regions (black square prisms) is 10^{-2} S m^{-1}, which is 100 times lower than in the rest of the cathode coating. It is apparent that the domain size modulates the intensity of MF patterns, while the domain location modulates the distribution of patterns. More examples are provided in SI (Fig. 2S)

3.2.5. Defect domain conductivity

Fig. 10 shows ΔB_{DC} maps of the disk-shaped domain, as in Fig. 5a, for a series of domain's conductivity values in the range from 10^{7} to 10^{-1} S m^{-1}. Local conductivity change in the cathode and electrolyte can manifest as two types of ΔB_{DC} patterns. If the defect conductivity is much higher than that of the surrounding material (1 S m^{-1}), the ΔB_{DC} map contains an anisotropically blurred image of the defect, *e.g.* Fig. 10a and b. In such cases, Surface-Scan MRI allows to identify X-Z coordinates and morphology of highly conductive regions readily. Similar effects are also demonstrated in Figs. 5 and 6. The second type of patterns resulting from local conductivity alterations manifests as half-oval features near the periphery of the image plane. Note, polarities of these patterns change when the defect conductivity falls below the nominal value of 1 S m^{-1}, transition between Fig. 10d and e.

A uniform decrease in conductivity of the electrolyte, e.g. as a result of degradation, leads to effects shown in Fig. 3S (SI). The effects are shown for conductivity values of 0.5 (a), 0.25 (b), 0.1 (c) and 0.01 S m^{-1} (d). The maximum $\Delta B_{DC} \sim 0.5$ μT is observed at the lowest conductivity (d) near the anode's terminal . Similarly, reducing the conductivity of the anode results in ΔB_{DC} field distribution shown in Fig. 4S (SI). As in the previous case, the maximum ΔB_{DC} magnitude (~ 0.12 μT) occurs at the anode's terminal.

ΔB_{DC} effects resulting from uniform degradation of the anode or the electrolyte are small (< 0.5 μT) compared to MF perturbations (6 – 70 μT) produced by "high conductivity" defects, Figs. 5–8. Thus, the former defect domains would be harder to detect. However, based on the outcomes of the previous experimental work [18] and with a potential sensitivity enhancement by means of specialized RF coil designs [30], the realistic sensitivity limit can approach ~ 1 μT.

The original experiments with 15-layer Nokia BL-5C cells ($D_Z = 53$ mm, $D_X = 34$ mm, $D_Y = 5$ mm) showed local ΔB_{DC} values ranging between 20 and 120 μT [18]. Note, as discussed above, experimental ΔB_{DC} maps[18] resulted from averaging over a 1 mm layer of the detection medium layer, and the MRI resolution was ~ 1.5 mm.

Experimental ΔB_{DC} maps of cells damaged by overcharging [18] contain features which by order of magnitude and spatial scales approach the MF distributions shown in Figs.5, Figs.6e, Figs.8c–g, Fig. 9e, and Fig. 10a-b. Thus, the experimental ΔB_{DC} patterns [18] could be associated with either relatively small (multiple mm) but highly conductive ($\sigma \sim 10^{6}$ - 10^{7} S m^{-1}) dendrite-rich domains, or with large (multiple cm) domains of degraded "low conductivity" cathode coating.

Although the main focus of this work is modeling of MRI measurables associated with cell's defects, similar considerations could also be used to examine potential applications of magnetometry towards battery diagnostics. Sensors such as atomic magnetometers allow detecting tiny magnetic field changes in response to changes of magnetic susceptibility and transient electrical currents [31].

Applications of atomic magnetometry for analysis of solid-state cells [32], and of nitrogen-vacancy-based magnetometry for examination of distributions of conducting elements [33] were also demonstrated. Measurements of current distributions were performed using fluxgate sensors [34] and anisotropic magnetoresistance sensors [35]. The calculations demonstrated in this work could be used to predict the detectability of defects in the magnetometry field as well. Magnetometry and MRI could be seen as complementary techniques with their own strengths and weaknesses. While MRI is generally less sensitive and more expensive, it provides faster measurements at high resolution and is less affected by sensor interference.

4. Conclusion

A range of fundamental problems associated with Li-ion cells is quite broad [36]. To minimize the release of defective cells to the market, both cell designs and pre-release diagnostic approaches should be improved. Even minor defects introduced during cell manufacturing are known to lead to inconsistent performance including different life spans of cells considered "identical". One of the strengths of Surface-Scan MRI is the ability to detect such performance variability in operando. ΔB_{DC} distribution is a key metric directly associated with charge - discharge processes. Stress factors such as overheating, over-charging, and over-discharging result in degradation of electrochemical components of cells, which in turn changes the current density and magnetic field distributions. Therefore, ΔB_{DC} represents local variations in current density induced by hazardous events. In this study, effects of morphology, location, and conductivity of the defect domain on ΔB_{DC} metrics were investigated numerically for the first time. We provided new insights into electromagnetic phenomena associated with operating battery cells, and validated Surface-Scan MRI as an informative analytical approach to cells diagnostics.

Declaration of Competing Interest

The authors declare no conflict of interest.

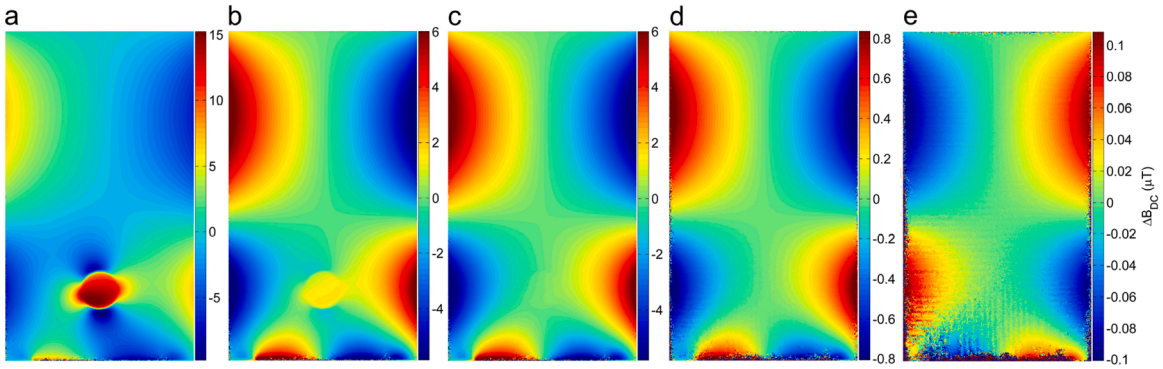

Fig. 10. ΔB_{DC} distribution as a function of conductivity of a disk-shaped defect domain located within the electrolyte and the cathode coating of a 1-layer cell. ΔB_{DC} maps are shown for defect conductivities of 10^{7} (a), 10^{6} (b), 10^{5} (c), 10 (d) and 10^{-1} S m^{-1} (e).

Supplementary materials

Supplementary material associated with this article can be found, in the online version, at doi:10.1016/j.jmro.2022.100061.

References

[1] J.R. Dahn, E.W. Fuller, M. Obrovac, U. Von Sacken, Thermal stability of Li_xCoO_2, Li_xNiO_2 and λ-MnO_2 and consequences for the safety of Li-ion cells, Solid State Ionics 69 (1994) 265–270.

[2] K. Kumai, H. Miyashiro, Y. Kobayashi, K. Takei, R. Ishikawa, Gas generation mechanism due to electrolyte decomposition in commercial lithium-ion cell, J. Power Sources 81-82 (1999) 715–719.

[3] Ph. Biensan, B. Simon, J.P. Peres, A. de Guibert, M. Broussely, J.M. Bodet, F. Perton, On safety of lithium-ion cells, J. Power Sources 81–82 (1999) 906–912.

[4] D.D. MacNeil, J.R. Dahn, The reactions of $Li_{0.5}CoO_2$ with nonaqueous solvents at elevated temperatures, J. Electrochem. Soc. 149 (2002) A912.

[5] H. Maleki, J.N. Howard, Effects of overdischarge on performance and thermal stability of a Li-ion cell, J. Power Sources 160 (2006) 1395–1402.

[6] D. Belov, M.-.H. Yang, Failure mechanism of Li-ion battery at overcharge conditions, J. Solid State Electrochem. 12 (2008) 885–894.

[7] D. Belov, M.H. Yang, Investigation of the kinetic mechanism in overcharge process for Li-ion battery, Solid State Ionics 179 (2008) 1816–1821.

[8] S.M. Rezvanizaniani, Z. Liu, Y. Chen, J. Lee, Review and recent advances in battery health monitoring and prognostics technologies for electric vehicle (EV) safety and mobility, J. Power Sources 256 (2014) 110–124.

[9] C. Hendricks, N. Williard, S. Mathew, M. Pecht, A failure modes, mechanisms, and effects analysis (FMMEA) of lithium-ion batteries, J. Power Sources 297 (2015) 113–120.

[10] S. Abada, G. Marlair, A. Lecocq, M. Petit, V. Sauvant-Moynot, F. Huet, Safety focused modeling of lithium-ion batteries: a review, J. Power Sources 306 (2016) 178–192.

[11] Q. Wang, B. Mao, S.I. Stoliarov, J. Sun, A review of lithium ion battery failure mechanisms and fire prevention strategies, Prog. Energy Combustion Sci. 73 (2019) 95–131.

[12] J.P. Pender, G. Jha, D. Hyun Youn, J.M. Ziegler, I. Andoni, E.J. Choi, A. Heller, B. S. Dunn, P.S. Weiss, R.M. Penner, C.B. Mullins, Electrode degradation in lithium-ion batteries, ACS Nano 14 (2020) 1243–1295.

[13] S. Chen, Z. Gao, T. Sun, Safety challenges and safety measures of Li-ion batteries, Energy Sci. Eng. 9 (2021) 1647–1672.

[14] Y. Yang, R. Fu, H. Huo, The Methodology of Electrochemical In-Situ NMR and MRI, The Royal Society of Chemistry, Cambridge, United Kingdom, 2021.

[15] A.J. Ilott, M. Mohammadi, C.M. Schauerman, M.J. Ganter, A. Jerschow, Rechargeable lithium-ion cell state of charge and defect detection by in-situ inside-out magnetic resonance imaging, Nat. Commun. 9 (2018) 1776.

[16] K. Romanenko, A. Jerschow, Distortion-free inside-out imaging for rapid diagnostics of rechargeable Li-ion cells, Proc. Natl. Acad. Sci 116 (2019) 18783–18789.

[17] K. Romanenko, P.W. Kuchel, A. Jerschow, Accurate visualization of operating commercial batteries using specialized magnetic resonance imaging with magnetic field sensing, Chem. Mater. 32 (2020) 2107–2113.

[18] K. Romanenko, A. Jerschow, Observation of memory effects associated with degradation of rechargeable lithium-ion cells using ultrafast surface-scan magnetic resonance imaging, J. Mater. Chem. A 9 (2021) 21078–21084.

[19] M. Halse, J. Rioux, S. Romanzetti, J. Kaffanke, B. MacMillan, I. Mastikhin, N. J. Shah, E. Aubanel, B.J. Balcom, Centric scan SPRITE magnetic resonance imaging: optimization of SNR, resolution, and relaxation time mapping, J. Magn. Reson. 169 (2004) 102–117.

[20] M.A. Bernstein, K.F. King, X.J. Zhou, Handbook of MRI Pulse Sequences, Elsevier, Oxford, 2004.

[21] M.J. Graves, D.G. Mitchell, Body MRI artifacts in clinical practice: a physicist's and radiologist's perspective, J. Magn. Reson. Imag. 38 (2013) 269–287.

[22] J.R. Reichenbach, R. Venkatesan, D.A. Yablonskiy, M.R. Thompson, S. Lai, E. M. Haacke, Theory and application of static field inhomogeneity effects in gradient-echo imaging, J. Magn. Reson. Imag. 7 (1997) 266–279.

[23] J.T. Dudley, D.P. Wilkinson, G. Thomas, R. LeVae, S. Woo, H. Blom, C. Horvath, M. W. Juzkow, B. Denis, P. Juric, P. Aghakian, J.R. Dahn, Conductivity of electrolytes for rechargeable lithium batteries, J. Power Sources 35 (1991) 59–82.

[24] P.N. Nirmalraj, T. Lutz, S. Kumar, G.S. Duesberg, J.J. Boland, Nanoscale mapping of electrical resistivity and connectivity in graphene strips and networks, Nano Lett. 11 (2011) 16–22.

[25] M. Hotta, M. Hayashi, M.T. Lanagan, D.K. Agrawal, K. Nagata, Complex permittivity of graphite, carbon black and coal powders in the ranges of X-band frequencies (8.2 to 12.4 GHz) and between 1 and 10 GHz, ISIJ Int. 51 (2011) 1766–1772.

[26] M. Park, X. Zhang, M. Chung, G.B. Less, A.M. Sastry, A review of conduction phenomena in Li-ion batteries, J. Power Sources 195 (2010) 7904–7929.

[27] X.Y. Qiu, Q.-.C. Zhuang, Q.-.Q. Zhang, R. Cao, P.-.Z. Ying, Y.-.H. Qiang, S.-.G. Sun, Electrochemical and electronic properties of $LiCoO_2$ cathode investigated by galvanostatic cycling and EIS, Phys. Chem. Chem. Phys. 14 (2012) 2617–2630.

[28] E. Quartarone, P. Mustarelli, Review—emerging trends in the design of electrolytes for lithium and post-lithium batteries, J. Electrochem. Soc. 167 (2020), 050508.

[29] D.S. Hall, J. Self, J.R. Dahn, Dielectric constants for quantum chemistry and li-ion batteries: solvent blends of ethylene carbonate and ethyl methyl carbonate, Phys. Chem. C 119 (2015) 22322–22330.

[30] B.J. Walder, M.S. Conradi, J.J. Borchardt, L.C. Merrill, E.G. Sorte, et al., NMR spectroscopy of coin cell batteries with metal casings, Sci. Adv. 7 (2021) eabg8298.

[31] Y. Hu, G.Z. Iwata, M. Mohammadi, E.V. Silletta, A. Wickenbrock, J.W. Blanchard, D. Budker, A. Jerschow, Sensitive magnetometry reveals inhomogeneities in charge storage and weak transient internal currents in Li-ion cells, Proc. Nat. Acad. Sci. 117 (2020) 10667–10672.

[32] Y. Hu, et al., Rapid online solid-state battery diagnostics with optically pumped magnetometers, Appl. Sci. 10 (2020) 7864.

[33] X. Zhang, G. Chatzidrosos, Y. Hu, H. Zheng, A. Wickenbrock, A. Jerschow, D. Budker, Battery characterization via eddy-current imaging with nitrogen-vacancy centers in diamond, Appl. Sci. 11 (2021) 3069.

[34] M.G. Bason, T. Coussens, M. Withers, C. Abel, G. Kendall, P. Kruger, Non-invasive current density imaging of lithium-ion batteries, arXiv preprint (2021) arXiv: 2103.03358.

[35] F. Brauchle, F. Grimsmann, O. Kessel, K.P. Birke, Direct measurement of current distribution in lithium-ion cells by magnetic field imaging, J. Power Sources 507 (2021), 230292.

[36] J.S. Edge, S. O'Kane, R. Prosser, N.D. Kirkaldy, A.N. Patel, et al., Lithium ion battery degradation: what you need to know, Phys. Chem. Chem. Phys. 23 (2021) 8200–8221.